An all-silicon Raman laser

Haisheng Rong[1], Ansheng Liu[1], Richard Jones[1], Oded Cohen[2], Dani Hak[2], Remus Nicolaescu[1], Alexander Fang[1] & Mario Paniccia[1]

[1]*Intel Corporation, 2200 Mission College Blvd, CHP3-109, Santa Clara, California 95054, USA*
[2]*Intel Corporation, S.B.I. Park Har Hotzvim, Jerusalem, 91031, Israel*

The possibility of light generation and/or amplification in silicon has attracted a great deal of attention[1] for silicon-based optoelectronic applications owing to the potential for forming inexpensive, monolithic integrated optical components. Because of its indirect bandgap, bulk silicon shows very inefficient band-to-band radiative electron–hole recombination. Light emission in silicon has thus focused on the use of silicon engineered materials such as nanocrystals[2–5], Si/SiO_2 superlattices[6], erbium-doped silicon-rich oxides[7–10], surface-textured bulk silicon[11] and Si/SiGe quantum cascade structures[12]. Stimulated Raman scattering (SRS) has recently been demonstrated as a mechanism to generate optical gain in planar silicon waveguide structures[13–21]. In fact, net optical gain in the range 2–11 dB due to SRS has been reported in centimetre-sized silicon waveguides using pulsed pumping[18–21]. Recently, a lasing experiment involving silicon as the gain medium by way of SRS was reported, where the ring laser cavity was formed by an 8-m-long optical fibre[22]. Here we report the experimental demonstration of Raman lasing in a compact, all-silicon, waveguide cavity on a single silicon chip. This demonstration represents an important step towards producing practical continuous-wave optical amplifiers and lasers that could be integrated with other optoelectronic components onto CMOS-compatible silicon chips.

The silicon Raman laser described here is based on a low-loss single-mode rib waveguide containing a reverse-biased p-i-n diode structure. The silicon rib waveguide is fabricated on the (100) surface of an undoped silicon-on-insulator (SOI) substrate. Silicon waveguide patterning was done using standard projection photolithography and Cl_2/Ar-based plasma reactive ion etching. A diagram of the waveguide cross-section is shown in Fig. 1a. The rib waveguide width (W), rib height (H) and etch depth (h) are (in μm) 1.5, 1.55 and 0.7, respectively. The effective core area[23] of the waveguide is calculated to be ~1.6 μm^2 by using a fully vectorial waveguide modal solver FIMMWAVE (details available at http://www.photond.com/products/fimmwave.htm). The waveguide is formed in an S-shaped curve with a bend radius of 400 μm and a total length of 4.8 cm (Fig. 1b). The straight sections of the waveguide are oriented along the [011] direction. The linear optical transmission loss of the S-bend waveguide was measured to be $0.35 \pm 0.05\ dB\ cm^{-1}$ on the basis of Fabry–Pérot resonance measurements[24] of a polished but uncoated waveguide.

The silicon Raman laser optical cavity was formed by coating one of the waveguide facets with a multi-layer coating while leaving the other facet uncoated. The facet coating was designed to be broadband and have a high reflectivity (~90%) for both the pump wavelength of 1.536 μm and the Raman/Stokes wavelength of 1.67 μm. The uncoated facet has a reflectivity of ~30% for both pump and Raman wavelengths. The pump beam is coupled into the cavity through the uncoated facet (see Fig. 1b). Although the laser beam is emitted from both facets of the silicon chip, we measured the laser output only from the uncoated facet. The waveguide loss was measured before the application of the multi-layer coating to the waveguide facet. The coating reflectivity was determined by measuring the linear optical transmission spectrum of the same waveguides before and after application of the coating.

Figure 1b shows the experimental set-up. An external cavity continuous-wave (c.w.) diode laser at 1.536 μm is amplitude modulated using an acousto-optic modulator to produce square-wave pulses of ~130 ns width at 10 kHz. An erbium-doped fibre amplifier system of three gain stages is used to amplify these pulses to produce a pump beam of peak power up to 2 W. The pump beam passes through a thin-film-based wavelength de-multiplexer and is coupled into the waveguide cavity by a lensed fibre. The Raman laser output and the reflected pump beam are coupled back into the lensed fibre, and separated through the wavelength de-multiplexer. The extracted laser output from the reflection port of the de-multiplexer is further filtered by a double-grating monochromator before being detected by a power meter or photodetector. The coupling loss between the lensed fibre and the waveguide was measured to be ~4 dB, the insertion loss of the de-multiplexer is 0.6 dB, and the monochromator has a loss of 6.7 dB.

One of the main limiting factors for achieving net gain, and hence lasing, from SRS in silicon waveguides is two-photon generated free carrier absorption (FCA). As has been shown previously[15,17], under

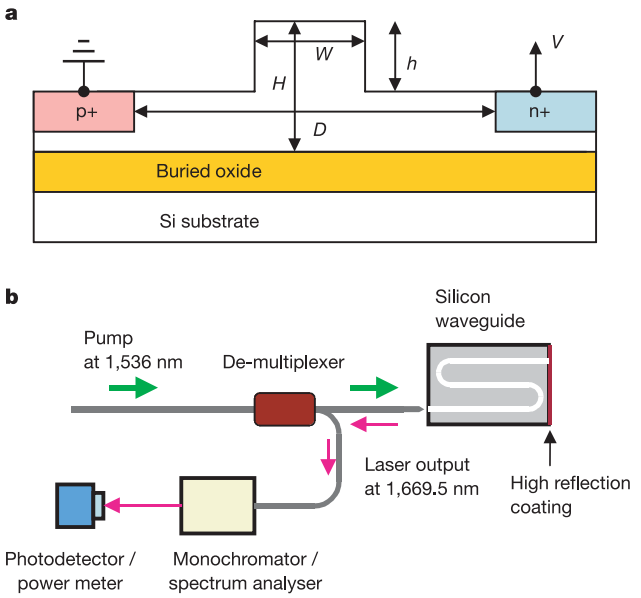

Figure 1 Diagrams showing silicon waveguide laser cavity and experimental set-up. **a**, Cross-section of a silicon-on-insulator (SOI) rib waveguide containing a reverse biased p-i-n diode structure with an applied voltage of V. **b**, Set-up for Raman lasing experiment. See main text for details.

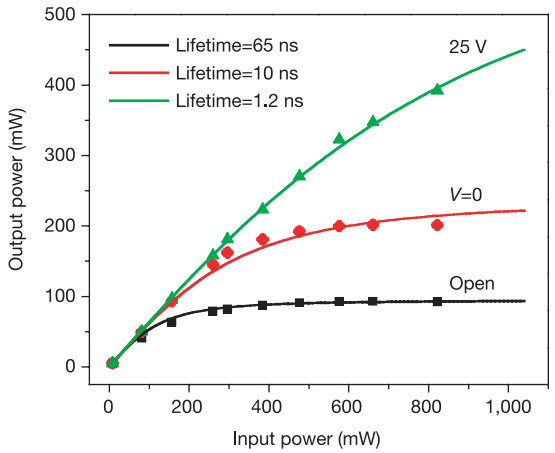

Figure 2 Nonlinear optical transmission of a 4.8-cm-long silicon waveguide containing a p-i-n diode with and without reverse bias. The symbols represent the experimental results and the curves the modelled results. 'Lifetime' indicates effective carrier lifetime.

high-power excitation two photon absorption (TPA) in silicon[25,26] induces a significant amount of free carriers because of the relatively long carrier recombination lifetime. These photogenerated free carriers induce additional optical loss owing to the free carrier plasma dispersion effect, otherwise known as FCA[27]. This FCA is problematic, as it both attenuates the pump beam and increases the optical loss for the Raman signal. To reduce such an effect, we designed a p-i-n diode structure along the rib waveguide. The silicon rib waveguide has heavily doped p- and n-type regions in the silicon slab (Fig. 1a). The separation between the p- and n-doped regions is $D = 6\,\mu m$. The p and the n sections of the diode were formed by boron and phosphorus implantation. The implantation dose, energy and thermal treatment resulted in a surface doping concentration of $\sim 1 \times 10^{20}\,cm^{-3}$ as well as small lateral diffusion to minimize interaction with the optical mode. Aluminium films were deposited on the p- and n-doped surface regions to form ohmic contacts (not shown in Fig. 1a) followed by a SiO_2 passivation layer. Our modelling and testing confirm that the linear optical loss of the waveguide is not affected by the heavily doped regions and metal contacts.

When a reverse bias is applied to the p-i-n diode, the TPA-generated electron–hole pairs can be swept out of the silicon waveguide between the p- and n-doped regions by the applied electric field. Thus the carrier transit time or effective carrier lifetime can be modified by the reverse bias voltage. To verify this experimentally, we measured the transmitted power of an anti-reflection-coated silicon p-i-n diode waveguide as a function of the c.w. input power with various reverse bias voltages. The experimental results are shown in Fig. 2. The symbols represent the measured data, and the solid curves are the modelled results based on the formalism described in ref. 17. There is a good agreement between modelled and measured results. As can be seen, the transmitted power for a silicon waveguide saturates to a given level as the input power is increased. This is a result of TPA-induced FCA. Increasing the bias voltage on the p-i-n diode allows the transmission of the device to be improved. In the modelling, the carrier lifetime is used as a fitting parameter. The linear optical loss is $\sim 0.35\,dB\,cm^{-1}$, the TPA coefficient is $0.5\,cm\,GW^{-1}$ (ref. 14) and the FCA cross-section is $1.45 \times 10^{-17}\,cm^2$ at the wavelength of $1.55\,\mu m$ (refs 24, 27). The anode (p-type region) of the p-i-n is always connected to ground. When the p-i-n diode circuit is open (that is, the p- and n-doped regions are not wire connected so that no net current is flowing), significant saturation in transmission is observed, and the modelled carrier lifetime is 65 ns. When the p-i-n diode circuit is closed (current flow is allowed but the bias voltage is zero), transmission is clearly improved, and the modelled carrier lifetime is 10 ns. When the p-i-n diode is reverse biased with a voltage of 25 V, the power transmission is further improved, and the corresponding carrier lifetime becomes 1.2 ns. These results show that the nonlinear loss due to the TPA-induced FCA is much reduced by shortening the carrier lifetime using the reverse biased p-i-n diode structure.

The single-pass Raman gain is measured for a silicon p-i-n waveguide with anti-reflection coatings on both facets using the techniques described in refs 17 and 18. With a reverse bias of 25 V applied to the p-i-n waveguide, a single-pass peak on-off gain of 5.2 dB is obtained, which is sufficient to achieve lasing in the cavity described above with a total round-trip loss of 9 dB. From these gain measurements, the Raman gain coefficient is estimated to be $\sim 7.5\,cm\,GW^{-1}$ using the method given in ref. 18.

Figure 3 shows the average power of the laser output measured from the uncoated side of the silicon waveguide cavity with a reverse bias of 25 V as a function of average pump power into the waveguide cavity, as depicted in Fig. 1b. As can be seen from Fig. 3, the laser threshold is at ~ 0.4 mW, and the slope efficiency (single side output) is 9.4%. Including the laser output from the other facet with 90% reflectivity, we estimate the total slope efficiency to be $\sim 10\%$. At a pump power > 0.9 mW, the laser output starts to saturate. This mainly results from the fact that the free carrier lifetime is of the order of ~ 1 ns and nonlinear loss due to the TPA-induced FCA reduces the net gain at high pump powers.

At a pump power of 0.7 mW, we measured the spectrum of the Raman laser from the waveguide cavity. The measurement results are shown in Fig. 4a. For comparison we also show the spectrum of the spontaneous Raman emission taken on an identical waveguide but without the highly reflective coatings. We see from Fig. 4a that the laser spectral width is much narrower than that of the spontaneous emission spectrum. Figure 4b is a higher-resolution

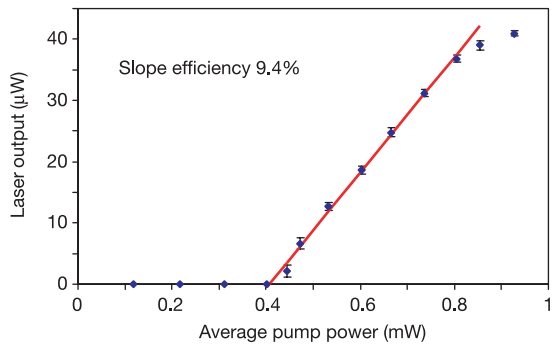

Figure 3 Average output of the silicon Raman laser with reverse biased p-i-n diode as a function of the average pump power into the silicon waveguide cavity. The input pump wavelength is 1,536 nm and the output Raman laser wavelength is 1,669.5 nm. The reverse bias voltage is 25 V. The slope efficiency (single side output) is 9.4%. Error bars represent standard deviations.

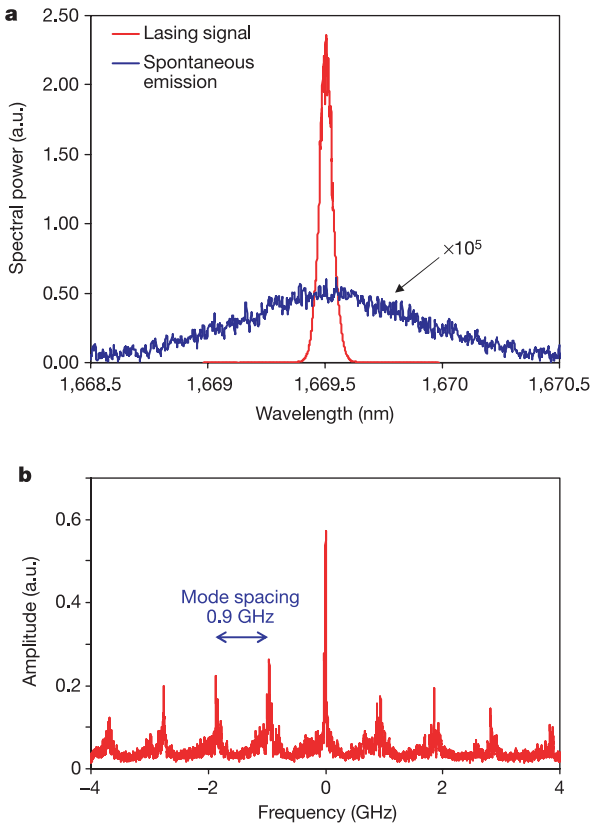

Figure 4 Silicon Raman laser spectra. **a**, Laser spectrum at an average pump power of 0.7 mW (red trace). For comparison, the blue trace shows the spontaneous Raman emission spectrum from a waveguide without a cavity. Note the different vertical scales. **b**, High-resolution Raman laser spectrum measured with a scanning Fabry–Pérot interferometer, showing resolved cavity modes.

spectrum of the laser using a scanning Fabry–Pérot spectrum analyser. We see that the laser has multiple cavity modes with a mode spacing of ~0.9 GHz, which corresponds to the free spectral range of a 4.8-cm-long silicon waveguide cavity.

This demonstration of Raman lasing in a silicon waveguide cavity on a single chip represents a significant step towards a more practical, all-silicon-based, c.w. amplifier or laser. We note that the multi-layer coatings are not essential for this device, and that single chip resonators may be fabricated using waveguide Bragg reflectors or ring resonator architectures; both these alternatives are compatible with CMOS processing. Further reduction in the carrier lifetime or cavity optimization could lead to c.w. Raman lasing in silicon. □

Received 23 October; accepted 10 December 2004; doi:10.1038/nature03273.
Published online 5 January 2005.

1. Pavesi, L., Gaponenko, S. & Dal Negro, L. (eds) *Towards the First Silicon Laser* (NATO science series, Kluwer, Dordrecht, 2003).
2. Shimizu-Iwayama, T. *et al.* Visible photoluminescence in Si^+-implanted silica glass. *J. Appl. Phys.* **75,** 7779–7783 (1994).
3. Brongersma, M. L., Polman, A., Min, K. S., Tambo, T. & Atwater, H. A. Tuning the emission wavelength of Si nanocrystals in SiO_2 by oxidation. *Appl. Phys.* **72,** 2577–2579 (1998).
4. Iacona, F., Franzo, G. & Spinella, C. Correlation between luminescence and structural properties of Si nanocrystals. *J. Appl. Phys.* **87,** 1295–1303 (2000).
5. Pavesi, L., Negro, L. D., Mazzoleni, C., Franzo, G. & Priolo, F. Optical gain in silicon nanocrystals. *Nature* **408,** 440–444 (2000).
6. Lockwood, D. J., Lu, Z. H. & Baribeau, J. M. Quantum confined luminescence in Si/SiO_2 superlattices. *Phys. Rev. Lett.* **76,** 539–541 (1996).
7. Lombardo, S., Campisano, S. U., van den Hoven, G. N., Cacciato, A. & Polman, A. Room-temperature luminescence from Er^{3+}-implanted semi-insulating polycrystalline silicon. *Appl. Phys. Lett.* **63,** 1942–1944 (1993).
8. Fujii, M., Yoshida, M., Kanzawa, Y., Hayashi, S. & Yamamoto, K. 1.54 μm photoluminescence of Er^{3+} doped into SiO_2 films containing Si nanocrystals: evidence for energy transfer from Si nanocrystals to Er^{3+}. *Appl. Phys. Lett.* **71,** 1198–1200 (1997).
9. Kik, P. G., Brongersma, M. L. & Polman, A. Strong exciton-erbium coupling in Si nanocrystal-doped SiO_2. *Appl. Phys. Lett.* **76,** 2325–2327 (2000).
10. Han, H. S., Seo, S. Y. & Shin, J. H. Optical gain at 1.54 μm in erbium-doped nanocluster sensitized waveguide. *Appl. Phys. Lett.* **79,** 4568–4570 (2001).
11. Trupke, T., Zhao, J., Wang, A., Corkish, R. & Green, M. Very efficient light emission from bulk crystalline silicon. *Appl. Phys. Lett.* **82,** 2996–2998 (2003).
12. Dehlinger, G. *et al.* Intersubband electroluminescence from silicon-based quantum cascade structures. *Science* **290,** 2277–2280 (2000).
13. Claps, R., Dimitropoulos, D., Han, Y. & Jalali, B. Observation of Raman emission in silicon waveguides at 1.54 μm. *Opt. Express* **10,** 1305–1313 (2002).
14. Claps, R., Dimitropoulos, D., Raghunathan, V., Han, Y. & Jalali, B. Observation of stimulated Raman amplification in silicon waveguides. *Opt. Express* **11,** 1731–1739 (2003).
15. Liang, T. K. & Tsang, H. K. Role of free carriers from two-photon absorption in Raman amplification in silicon-on-insulator waveguides. *Appl. Phys. Lett.* **84,** 2745–2747 (2004).
16. Espinola, R. L., Dadap, J. I., Osgood, R. M. Jr, McNab, S. J. & Vlasov, Y. A. Raman amplification in ultrasmall silicon-on-insulator wire waveguides. *Opt. Express* **12,** 3713–3718 (2004).
17. Rong, H. *et al.* Raman gain and nonlinear optical absorption measurement in a low loss silicon waveguide. *Appl. Phys. Lett.* **85,** 2196–2198 (2004).
18. Liu, A., Rong, H., Paniccia, M., Cohen, O. & Hak, D. Net optical gain in a low loss silicon-on-insulator waveguide by stimulated Raman scattering. *Opt. Express* **12,** 4261–4267 (2004).
19. Xu, Q., Almeida, V. & Lipson, M. Time-resolved study of Raman gain in highly confined silicon-on-insulator waveguides. *Opt. Express* **12,** 4437–4442 (2004).
20. Liang, T. K. & Tsang, H. K. Efficient Raman amplification in silicon-on-insulator waveguides. *Appl. Phys. Lett.* **85,** 3343–3345 (2004).
21. Boyraz, O. & Jalali, B. Demonstration of 11dB fiber-to-fiber gain in a silicon Raman amplifier. *IEICE Elect. Express* **1,** 429–434 (2004).
22. Boyraz, O. & Jalali, B. Demonstration of a silicon Raman laser. *Opt. Express* **12,** 5269–5273 (2004).
23. Agrawal, G. P. *Nonlinear Fiber Optics* 2nd edn (Academic, New York, 1995).
24. Reed, G. T. & Knights, A. P. *Silicon Photonics: An Introduction* (John Wiley, Chichester, UK, 2004).
25. Tsang, H. K. *et al.* Optical dispersion, two photon absorption and self-phase modulation in silicon waveguides at 1.5 μm wavelength. *Appl. Phys. Lett.* **80,** 416–418 (2002).
26. Dinu, M., Quochi, F. & Garcia, H. Third-order nonlinearities in silicon telecom wavelengths. *Appl. Phys. Lett.* **82,** 2954–2956 (2003).
27. Soref, R. A. & Lorenzo, P. J. All-silicon active and passive guided-wave components for λ = 1.3 and 1.6 μm. *IEEE J. Quant. Electron.* **QE-22,** 873–879 (1986).

Acknowledgements We thank A. Alduino, D. Tran, J. Tseng, D. Hodge and J. Johnson for assistance in device fabrication and sample preparation; S. Koehl for software development; M. Morse, H. Liu, M. Salib, D. Samararubio, L. Liao, R. Li and G. Ding for technical discussions; and G. T. Reed, I. P. Kaminow and J. E. Bowers for conversations.

Competing interests statement The authors declare that they have no competing financial interests.

Correspondence and requests for materials should be addressed to H.R. (haisheng.rong@intel.com).

Stable sea surface temperatures in the western Pacific warm pool over the past 1.75 million years

Thibault de Garidel-Thoron[1], Yair Rosenthal[1,2], Franck Bassinot[3] & Luc Beaufort[4]

[1]*Institute of Marine and Coastal Sciences-Rutgers University, 71 Dudley Road, and*
[2]*Department of Geological Sciences-Rutgers University, New Brunswick, New Jersey 08901, USA*
[3]*Laboratoire des Sciences du Climat et de l'Environnement–CEA, 91198 Gif-sur-Yvette cedex, France*
[4]*CEREGE-CNRS Université Aix-Marseille 3, BP80, 135345 Aix-en-Provence cedex 4, France*

About 850,000 years ago, the period of the glacial cycles changed from 41,000 to 100,000 years. This mid-Pleistocene climate transition has been attributed to global cooling, possibly caused by a decrease in atmospheric carbon dioxide concentrations[1,2]. However, evidence for such cooling is currently restricted to the cool upwelling regions in the eastern equatorial oceans[3,4], although the tropical warm pools on the western side of the ocean basins are particularly sensitive to changes in radiative forcing[5,6]. Here we present high-resolution records of sea surface temperatures spanning the past 1.75 million years, obtained from oxygen isotopes and Mg/Ca ratios in planktonic foraminifera from the western Pacific warm pool. In contrast with the eastern equatorial regions, sea surface temperatures in the western Pacific warm pool are relatively stable throughout the Pleistocene epoch, implying little long-term change in the tropical net radiation budget. Our results challenge the hypothesis of a gradual decrease in atmospheric carbon dioxide concentrations as a dominant trigger of the longer glacial cycles since 850,000 years ago. Instead, we infer that the temperature contrast across the equatorial Pacific Ocean increased, which might have had a significant influence on the mid-Pleistocene climate transition.

The warmest pool of oceanic surface lies in the western equatorial Pacific Ocean and plays an important role in Earth's climate. Annual sea surface temperatures (SSTs) above 28 °C (ref. 7) lead to deep atmospheric convection, which transfers through the atmosphere large amounts of water vapour and latent heat from tropical to mid-latitudes. The importance of the western equatorial Pacific warm pool (WPWP) is perhaps best manifested by the impact of the El Niño/Southern Oscillation (ENSO) on the interannual variability in the Earth's temperature and precipitation patterns[8,9]. ENSO-linked changes in tropical SST patterns also have a major influence on heat transport from low to mid- and high latitudes[10] and models suggest that long-term changes of SST patterns in the equatorial Pacific may also have had large consequences for extra-tropical climate in the past[11]. Thus, reconstructing past changes in tropical Pacific SSTs is critical for understanding the evolution of global heat and moisture transport, such as those occurring during the mid-Pleistocene transition, characterized by the onset of the large 100-kyr glacial cycles, about 0.85 Myr ago.

Here, we present a high-resolution Pleistocene record (0–1.75 Myr ago, Marine Isotopic Stages MIS1 to MIS59) of paired $\delta^{18}O$ and Mg/Ca measurements in planktonic foraminifera (*Globigerinoides ruber*, 250–300 μm, white) (Fig. 1) from the IMAGES core MD97-2140 located in the heart of the WPWP (2° 02′ N, 141° 46′ E, 2,547 m; Supplementary Fig. S1). The record extends the previously published, late-Pleistocene Ocean Drilling Program (ODP) site 806B record (0–450 kyr ago) from the Ontong-Java plateau[12], thus providing new insights on tropical Pacific climate variability during